

Space charge and plasma effects in zero kinetic energy (ZEKE) photoelectron spectroscopy

D. M. Villeneuve,^{a)} Ingo Fischer,^{b)} A. Zavriyev,^{c)} and Albert Stolow
*Steacie Institute for Molecular Sciences, National Research Council of Canada,
Ottawa Ontario K1A 0R6, Canada*

(Received 4 December 1996; accepted 2 July 1997)

In photoelectron spectroscopy experiments it is generally assumed that the Coulomb force between charged particles is small compared with external fields, and that the free kinetic electrons will quickly leave the ions. This is the basis of the ZEKE photoelectron spectroscopy. However as the density of charged particles is increased, plasma physics effects begin to become important, and the kinetic electrons become trapped by the net positive charge and move so as to set up a self-field which can cancel any externally imposed electric fields. For high densities, fewer electrons than expected are able to escape the self-field. The production of self-consistent electric fields is studied by means of particle-in-cell plasma simulations and by N -body trajectory calculations, and simple expressions are derived for when plasma physics effects become significant. An experimental illustration of plasma effects in ZEKE is presented. © 1997 American Institute of Physics. [S0021-9606(97)00838-6]

I. INTRODUCTION

Within the last ten years, zero kinetic energy (ZEKE) photoelectron spectroscopy, based on pulsed field ionization (PFI) of long-lived, high- n Rydberg states,^{1,2} has become an important spectroscopic technique for high resolution studies of molecular ions and for dynamical studies of excited states in both frequency³ and time domains.⁴⁻⁶

The success of the technique is based upon the fact that kinetic electrons quickly leave the collection region during a delay time (on the order of microseconds), leaving behind the high- n Rydberg states which are detected by pulsed electric field ionization. However, with each laser shot, many ions can be produced in the laser focus. These ions exert a Coulomb force on the free electrons which may in fact trap the low energy electrons in the ion cloud. When a delay pulsed electric field is applied, these trapped electrons obtain enough energy to escape the Coulomb potential of the plasma and are therefore detected, indistinguishable from a ZEKE signal.

These plasma effects have been reported on several occasions. For example in the $[1+1]$ ZEKE spectrum of para-difluorobenzene via the S_1 state,¹ several anomalous peaks appeared in the ZEKE spectrum which could be attributed to accidental resonances within the S_1 manifold. It was suggested that the large excess of ions produced by such accidental resonances led to the trapping of kinetic electrons. Recently, this phenomena was reported in the $[1+2]$ ZEKE spectrum of iodine, where accidental $[1,1]$ resonances also gave "false" ZEKE signals.⁷

These space charge effects are especially problematic in multiphoton experiments where the laser power, and hence

the number of ions, cannot be reduced below a certain limit. Furthermore, excess ion density is actually necessary in order to enhance Rydberg lifetimes⁸⁻¹⁰ and therefore it is usually not possible to arbitrarily reduce ion densities. The "line" between ion enhancement of ZEKE signals and the trapping of low kinetic energy electrons is blurred, of course, and therefore it is worthwhile to consider in more detail the plasma conditions required for such trapping.

In high-resolution ZEKE experiments, two kinds of plasma effects have been observed. When the ion density is too high, trapped kinetic electrons are always produced, independent of laser frequency, and it is not possible to record a sharp ZEKE spectrum. The other mechanism, discussed above, produces trapped kinetic electrons when the ion density is greatly enhanced at accidental intermediate state resonances. In high-resolution spectroscopy, it should be possible to discern true ZEKE signals from such accidental resonance due to the particular red shifting of the ZEKE spectrum with increasing pulsed field extraction strength: the "false ZEKE" signal cannot red shift due to the strict requirement of intermediate state resonance.

In the case of time-domain ZEKE experiments, by contrast, the broad bandwidth of femtosecond pulses prevents the observation of single lines in the ZEKE spectrum and, hence, greater care is required to discern "false ZEKE" signals from true PFI of Rydberg states. One way to do this is to compare the lifetime of the ZEKE signal with the "lifetime" of the ion cloud in the viewing region of the spectrometer:¹⁰ trapped kinetic electrons should persist as long as the ion cloud is present. Other possible methods might involve the use of microwave radiation, or pulsed electric and magnetic fields¹¹ to specifically interact with high- n Rydberg states.

A medium of interacting positively charged ions and free electrons is a plasma. It is therefore appropriate to describe the space charge effects in ZEKE experiments with concepts used in plasma physics. In this paper, we introduce the rel-

^{a)}Electronic address: David.Villeneuve@nrc.ca

^{b)}Present address: Laboratorium für Organische Chemie der ETH Zürich, Universitätsstr. 16, CH-8092, Zürich.

^{c)}Present address: Tectron Systems Division, Wilmington Massachusetts 01887.

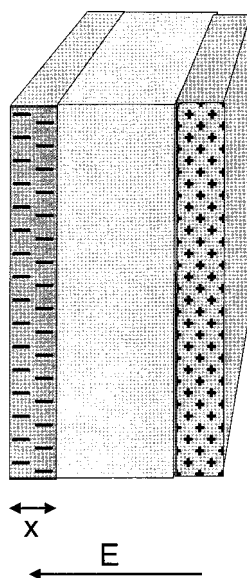


FIG. 1. Sketch of a sheet of plasma in which the electrons are separated from the ions by a small distance. The internal field generated by even a small separation can be surprisingly large.

evant plasma physics concepts and discuss the magnitude of the internal fields in terms of simple analytical models which provide convenient scaling laws for space charge effects. We then quantify the discussion using two kinds of plasma simulation techniques based upon particle-particle and particle-in-cell methods. Finally, we present a simple experimental illustration of plasma effects in ZEKE using three-photon non-resonant excitation of Xe.

We introduce several plasma physics concepts which are useful in the present context. A plasma is assumed to consist of a gas of ions and electrons which are free to travel in their self-consistent electric fields. The electrons and ions are assumed to have characteristic temperatures, T_e and T_i , which are related to their average random thermal velocity. Although in these simulations the velocity distributions are Maxwellian, this is not a necessary condition. The component particles have a local average number density, n_e and n_i ; for initial charge neutrality, $n_e = Zn_i$, where Z is the average ionic charge. In the following, we use SI units except where explicitly shown otherwise.

In order to estimate the magnitude of the self-generated electric field that a plasma can produce, consider a one-dimensional sheet of plasma as illustrated in Fig. 1. If the electrons are shifted a distance x from the ions (even if x is much less than the initial thickness of the sheet), the internal electric field is $E = en_e x / \epsilon_0$. For example, when $n_e = 10^{12} \text{ cm}^{-3}$ and $x = 1 \text{ } \mu\text{m}$, then the internal field is $E = 180 \text{ V/cm}$. This internal field is sufficient to counteract the force of most commonly-used external fields. If we were to fully separate this plasma with $n_e = 10^{12} \text{ cm}^{-3}$ and thickness $100 \text{ } \mu\text{m}$, then $E = 180 \text{ kV/cm}$! Clearly the electrons will be strongly bound to the ions.

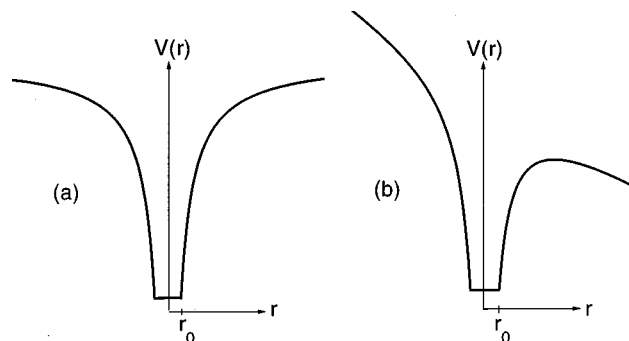


FIG. 2. Sketch of the potential of an cloud of ions with a net positive charge. (a) No external field. (b) The external electric field is applied.

II. ANALYTIC ESTIMATES

Consider a cloud of electrons and ions of radius r_0 . If N_{esc} electrons have escaped from the cloud, then the cloud will have a net positive charge eN_{esc} . Because of the very high electrical conductivity of a plasma, the electric field inside the cloud will be nearly zero. For $r > r_0$, the field will appear to be from a centrally located charge, as shown in Fig. 2(a). For an electron at the edge of the cloud to escape, its kinetic energy must exceed the local potential. This potential is given in terms of the number of electrons which have already escaped,

$$V = -\frac{eN_{esc}}{4\pi\epsilon_0 r}, \quad (1)$$

for $r > r_0$. If the electrons have an average kinetic energy T_e then electrons will be able to escape the ions' potential until the potential V equals T_e/e . Therefore the number of electrons which are able to escape is

$$N_{esc}(\text{sphere}) = \frac{4\pi\epsilon_0 r_0 T_e}{e^2} = 695 r_0 (\mu\text{m}) T_e (\text{eV}). \quad (2)$$

This simple expression shows that there is a limit to the number of electrons which can escape an ion cloud. (Obviously this expression requires that $N_{esc} < N_{total}$.)

In most experiments, the shape of the ion cloud is better described as a cylinder of length ℓ and radius r_0 . If we assume that the electric field varies as $1/r$ for $r < \ell$ and as $1/r^2$ for $r > \ell$, then (see Appendix A for details) the number of electrons which can escape is

$$N_{esc}(\text{cylinder}) = \frac{4\pi\epsilon_0 \ell T_e}{e^2} \frac{1}{1 + 2\ln\ell/r_0}. \quad (3)$$

We introduce a figure of merit parameter, f_{esc} , which is defined as the number of electrons which are able to escape the self-consistent fields divided by the number of electrons present. If $f_{esc} < 1$, then not all of the electrons can escape, and we then say that plasma effects are significant. If $f_{esc} \gg 1$, then plasma effects should be negligible. This is not to say that more electrons than are present will actually escape, but instead indicates that all electrons can freely escape if $f_{esc} \gg 1$. We therefore use $f_{esc} = 1$ as the dividing line between possible plasma problems and free escape.

In terms of the total number of free electrons N_{el} initially present in the cloud (N_{el} is n_e times the volume), the fraction of electrons which can escape the cloud is

$$\begin{aligned} f_{esc}(\text{sphere}) &= \frac{N_{esc}(\text{sphere})}{N_{el}(\text{sphere})} \\ &= \frac{3\epsilon_0 T_e}{e^2 n_e r_0^2} \\ &= 1.65 \times 10^{14} \frac{T_e(\text{eV})}{r_0^2(\mu\text{m}) n_e(\text{cm}^{-3})}, \end{aligned} \quad (4)$$

$$f_{esc}(\text{cylinder}) = \frac{N_{esc}(\text{cylinder})}{N_{el}(\text{cylinder})} = \frac{3\epsilon_0 T_e}{e^2 n_e r_0^2} \left(\frac{4/3}{1 + 2\ln L/r_0} \right), \quad (5)$$

where n_e is the average number density of free electrons initially in the cloud. Proportionately fewer electrons can escape a cylindrical cloud because the electric field scales as $1/r$ at close range.

It may seem counterintuitive that $N_{esc} \propto r_0$ but $f_{esc} \propto 1/r_0^2$. The former is a result of the fact that an electron at the edge of the cloud experiences a central force located a distance r_0 away, and therefore the probability of escape is proportional to r_0 . The latter scaling is a result of the fact that for a constant n_e , the total number of electrons initially in the cloud scales as $N_{el} \propto r_0^3$, and so there are many more electrons. In reality n_e will not stay constant as r_0 is increased: for a single-photon interaction, the number of electrons is proportional to laser pulse energy, not intensity, and so increasing the beam diameter will reduce n_e , increase N_{esc} , and increase f_{esc} .

If the number of electrons is greater than the limits in eqs. (4) and (5), then some electrons will be trapped by the self-consistent field set up by the ions. This can have a serious impact on ZEKE studies, where it is assumed that electrons above the ionization threshold will leave their parent ion and will leave the viewing region of the spectrometer. If there is another ionization channel that produces a large number of electrons exceeding N_{esc} , then some of these kinetic electrons will be trapped and will be indistinguishable from the Rydberg electrons when the pulsed field is turned on. In photoelectron spectroscopy experiments, a potential as small as 50 meV can be detrimental.

In many experiments an electric field is used to accelerate the charged particles into a mass spectrometer. What is the effect of an external electric field on the number of electrons that are able to escape? The field will have the effect of lowering the plasma barrier to electron escape, as illustrated in Fig. 2(b). It can be shown that, for a spherical cloud and an external electric field E_x ,

$$N_{esc}(\text{sphere}) = \frac{4\pi\epsilon_0 r_0^2}{e} (\sqrt{E_x} + \sqrt{T_e/er_0})^2, \quad (6)$$

$$f_{esc}(\text{sphere}) = \frac{N_{esc}(\text{sphere})}{N_{el}(\text{sphere})} = \frac{3\epsilon_0}{en_e r_0} (\sqrt{E_x} + \sqrt{T_e/er_0})^2. \quad (7)$$

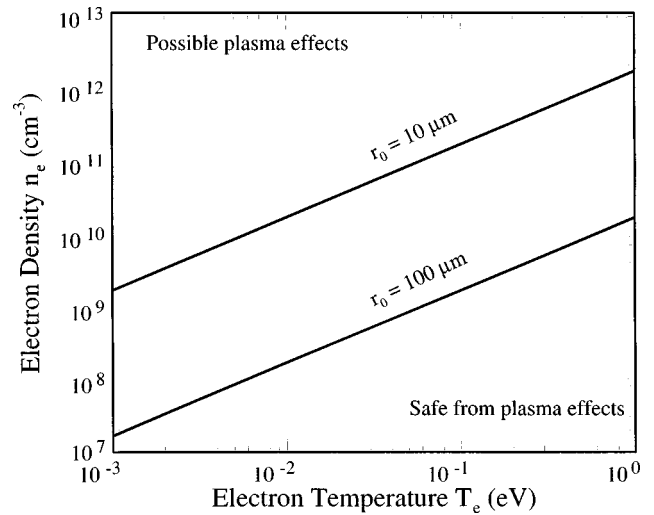


FIG. 3. Density limits below which electrons will leave a spherical ion cloud without the aid of an external field. The lines represent different radii of the initial ion cloud. Densities below the lines will generally be free from space charge effects.

In the limit of $E_x \rightarrow 0$, eq. (6) becomes eq. (2). In the limit of $E_x \gg T_e/er_0$, eqs. (6) and (7) become

$$N_{esc}(\text{sphere}) = \frac{4\pi\epsilon_0 r_0^2 E_x}{e}, \quad (8)$$

$$\begin{aligned} f_{esc}(\text{sphere}) &= \frac{N_{esc}(\text{sphere})}{N_{el}(\text{sphere})} \\ &= \frac{3\epsilon_0 E_x}{en_e r_0} \\ &= 1.65 \times 10^{10} \frac{E(\text{V/cm})}{n_e(\text{cm}^{-3}) r_0(\mu\text{m})}. \end{aligned} \quad (9)$$

These are the general conditions which govern the number of free electrons which will be able to escape the Coulomb field of the ions; electrons in excess of N_{esc} will be unable to escape and will be trapped in the ion cloud. In analogy with eq. (3), for a cylindrical distribution of charge, $N_{esc}(\text{cylinder})$ will be somewhat smaller than this.

In order to determine if self-fields are important for a particular experiment, use eq. (7); if $f_{esc} > 1$, then the Coulomb field can be neglected. The two limiting cases are illustrated in graphical form to show the electron densities above which space charge effects are possible. Figure 3 shows the densities at which $f_{esc}(\text{sphere}) = 1$ versus an electron kinetic energy in the limit of no external field. Figure 4 shows the densities at which $f_{esc}(\text{sphere}) = 1$ versus an external electric field in the limit of zero initial electron kinetic energy. In both graphs, densities below the line are generally safe from space-charge effects. The two graphs are to be used in conjunction: first determine from Fig. 3 if the electrons will leave on their own, and if n_e is too high for them to escape, use Fig. 4 to see what applied field is required to extract them.

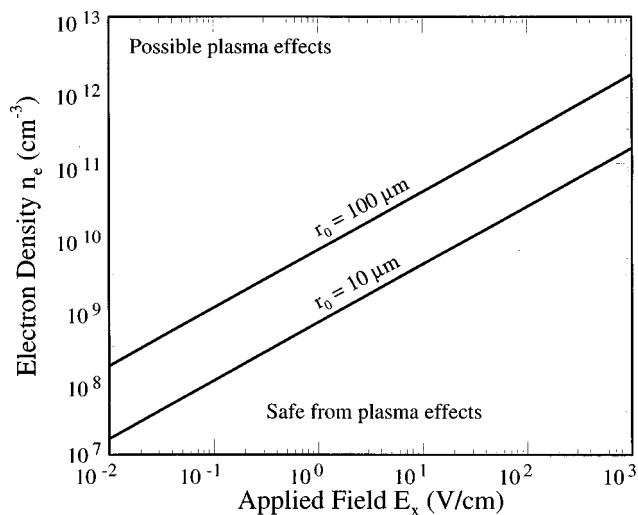


FIG. 4. Density limits below which electrons will leave a spherical ion cloud with an external field. The electrons are assumed to have zero kinetic energy, so they will not leave the ion cloud on their own. The lines represent different radii of the initial ion cloud. Densities below the lines will generally be free from space charge effects.

III. PARTICLE SIMULATIONS

The analytic results derived in the previous section are based on idealized assumptions such as that the problem is one dimensional, and that escaped electrons do not contribute to the electrical potential surrounding the ion cloud. Therefore, we investigated the applicability of these analytic estimates of escaped electrons by means of computer modelling.

There are various techniques used to model a plasma.¹² Hydrodynamic models treat the electrons and ions as collisional fluids. Vlasov models calculate the velocity distributions of the particles. Particle models use discrete particles to simulate the plasma. The particle model is best suited to dealing with an isolated plasma in an external electric field. Below we will present calculations based on two types of particle models.

In a particle simulation of a plasma, the simulation “particle” generally represents a number of real particles. A set of such particles is used, and the positions and velocities of the particles are tabulated. At discrete time steps, the self-consistent electromagnetic fields are calculated, and the particles are accelerated according to Maxwell’s equations and moved according to Newton’s laws.

Particle simulations are generally divided into two methods which differ only in the way that the fields are calculated: (1) particle–particle and (2) particle–mesh methods. In the particle–particle method, the force on a particle is calculated by considering the force from all other particles individually; the time for performing this type of calculation scales as N^2 , where N is the number of simulation particles. In particle–grid methods, the field is calculated on a spatial grid, and the force acting on a particle is derived from the field at its nearest grid point; this method scales as N , and so is more suited to calculations with large numbers of particles.

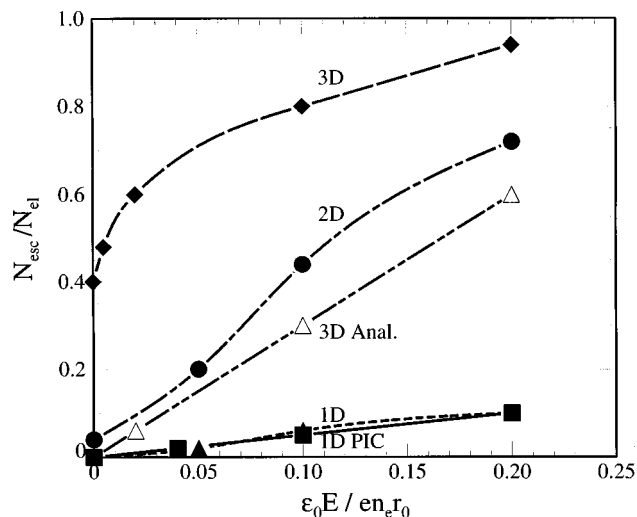


FIG. 5. Fraction of electrons which escape versus the external electric field. Results are shown for the particle–particle simulation in one, two and three dimensions, and for the one-dimensional particle-in-cell simulation. Also included is the analytical prediction in three dimensions.

The electron density n_e defines a characteristic frequency called the plasma frequency. This is the natural frequency at which an electron oscillates about an ion if disturbed from equilibrium: $\omega_p = (n_e e^2 / m_e \epsilon_0)^{1/2}$. The electron temperature and density define a characteristic distance called the Debye length, $\lambda_D = (\epsilon_0 T_e / n_e e^2)^{1/2}$. The Debye length is particularly significant because it is the distance over which electrons are able to shield out external fields. In practical units, $\lambda_D(\text{m}) = 7.43(T_e(\text{eV})/n_e(\text{cm}^{-3}))^{1/2}$. We use these parameters as our units of time and length.

We first discuss the particle–particle simulation, details of which are given in Appendix B. In order to study the effects of the size and shape of the plasma region, the code could operate in one, two or three dimensions. For the lower dimensions, the particles were assumed to be rods or sheets with a density corresponding to the density in the other dimension(s). For example, in two dimensions the plasma was an infinitely long cylinder with the electric field applied perpendicular to the cylinder axis.

Figure 5 shows the predictions of this model for different dimensionality. These results did not change when the number of electrons was changed. The usual numerical tests were done, for example changing the time step and changing the number of particles, to verify that the code was performing correctly.

Also shown in Fig. 5 is the prediction of eq. (7). The analytic model seems to better fit the 2D simulation, even though it assumes a spherical cloud and should fit the 3D simulation. In general, the analytic model seems to underestimate the number of escaped electrons compared with the simulation. Therefore our analytic estimates are conservative.

The simulation also showed that the shape of the charge distribution has an effect on the number of escaped electrons. In two dimensions, an elliptically shaped cylinder loses more electrons than a circular one, and if the long axis of the

ellipse is parallel to the electric field it loses about 20% more than if the long axis were perpendicular to the field.

The predictions of the simulation were also compared with a one-dimensional particle-in-cell plasma simulation. This technique, described in Appendix C, is faster than the particle–particle model and permitted calculations with larger numbers of electrons, but is limited to one dimension. Its predictions agree very well with the particle–particle model's in one dimension, and are shown in Fig. 5.

IV. IMPLICATIONS FOR PHOTOIONIZATION EXPERIMENTS

The results of the preceding sections indicate that too many ions in the laser focus can alter photoelectron kinetic energy distributions and trap low energy electrons in the self-generated potential. The signs of space charge effects are readily apparent in time-of-flight photoelectron spectroscopy: the sharp features in the spectra become blurred. In ZEKE photoelectron spectroscopy, however, the electron energies are not measured and therefore greater care is required to avoid trapping. For field-free escape of electrons, it must be ensured that [cf. eq. (4)]

$$n_e(\text{cm}^{-3}) \ll 1.65 \times 10^{14} \frac{T_e(\text{eV})}{r_0^2(\mu\text{m})}. \quad (10)$$

When an electric field is present (stray or applied), the condition becomes, in the limiting case of eq. (9) for $E_x \gg T_e/er_0$,

$$E_x(\text{V/cm}) \gg 6.06 \times 10^{11} r_0(\mu\text{m}) n_e(\text{cm}^{-3}). \quad (11)$$

This can be a severe constraint, since for $E_x = 100$ mV/cm and $r_0 = 50$ μm , $n_e \ll 3 \times 10^7$ cm^{-3} . Ion densities in typical experiments are 4×10^6 cm^{-3} .^{13,14}

Furthermore, since the field-free escape probability is proportional to T_e , the more energetic electrons escape first and set up a self-consistent field which can trap a larger number of slow electrons. It is conceivable that this can result in the observation of charge transfer between ions; Alt *et al.*¹³ observed MATI signals from C_6D_6 when C_6H_6 was excited to high Rydberg states, from which they inferred that charge transfer between Rydberg molecules occurred.

In ZEKE experiments the many ions and electrons that are produced by excitation to continuum states must be considered, since these can easily outnumber the ZEKE electrons which are in high-lying Rydberg orbitals. It is these free electrons which lead to the n_e that is used in eqs. (10) and (11). The very small spoiling field which is usually applied (intentionally or otherwise) to the plasma to remove these non-ZEKE electrons must be sufficient to extract almost all of them, otherwise they will be extracted by the larger pulsed field that is used to field-ionize the Rydberg electrons. Any non-ZEKE electrons which are not removed by the spoiling field will appear in the ZEKE signal as a background. If these free electrons are produced by some resonant mechanism then they will contribute peaks to the ZEKE spectrum which cannot be separated from the true

ZEKE signal except by a prior knowledge of the resonance. The magnitude of the spoiling field must satisfy eq. (11).

Reiser *et al.*¹ report that non-ZEKE signals can appear in ZEKE experiments. In the [1+1] ZEKE spectrum of *p*-difluorobenzene via the S1 state, they attributed several spectral peaks to large numbers of non-ZEKE electrons being produced by resonances with the S1 state. These excess electrons exceeded the number which could escape the space charge, and hence were detected along with the true Rydberg electrons.

How does one test for the presence of these plasma effects? For the case of a single ionization channel, increasing the gas density should result in a linear increase in ZEKE signal; a faster-than-linear increase is indicative of space charge effects. In the case of ZEKE studies where there is a competing ionization channel, both laser power and gas density must be checked for linearity of signal.

Space charge effects in ZEKE experiments are almost indistinguishable from ion interactions which enhance the lifetime of Rydberg states.¹⁵ Interactions of Rydberg states with surrounding ions are needed in order to increase the orbital angular momentum of Rydberg electrons to extend their lifetime sufficiently to be detected. Such ion effects have been observed experimentally.¹⁰ However, at higher densities, it may be that increasing the number of background ions simply traps some very low kinetic energy electrons in the ion cloud, and that it is these electrons, rather than the true Rydberg electrons, that are detected.

V. EXPERIMENTAL DEMONSTRATION OF PLASMA EFFECTS

In order to illustrate the type of plasma effects discussed in the preceding sections, we have performed three-photon ZEKE experiments using tunable femtosecond UV pulses on atomic Xe in the presence of excess ions. Previous experiments on three-photon ZEKE were performed to determine if the ZEKE technique could be used to selectively detect atoms using intense, short-pulse lasers.¹⁶ It should be noted that these experiments are qualitatively very different from conventional high-resolution ZEKE experiments using narrow-linewidth nanosecond lasers.

In the experiment, intense sub-picosecond pulses of laser light, tunable in a range around 306 nm, were used to excite xenon atoms. Non-resonant three-photon absorption of 306.5 nm light will excite xenon to its ionization potential (IP) of 12.130 eV. Because it is a third order effect, the ionization rate is a non-linear function of the laser intensity. Furthermore, the high laser intensities used (10^{12} – 10^{13} W/cm²) cause a significant ac Stark shift of the IP. The Stark shift is equal to the ponderomotive potential,

$$U_p = e^2 E_0^2 / 4m_e \omega^2 \quad (12)$$

where E_0 is the electric field of the laser, m_e is the electron mass and ω is the angular frequency of the laser. At a laser wavelength of 305 nm and in practical units, $U_p(\text{cm}^{-1}) = 70I(\text{W/cm}^2)/10^{12}$. This Stark shift is greater than the three-photon energy bandwidth of 200 cm^{-1} . (The measured

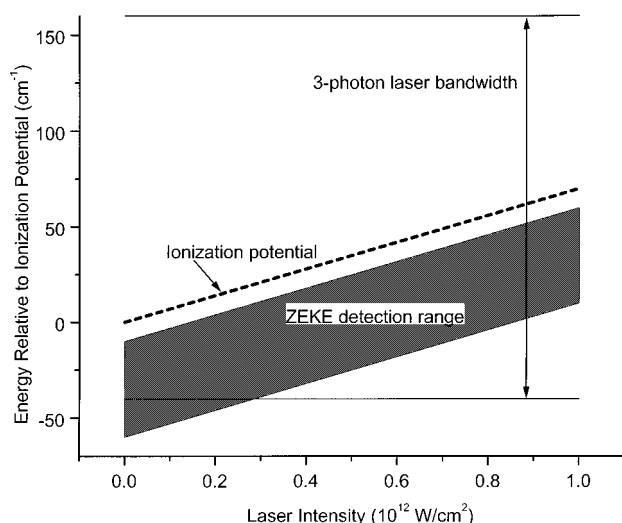


FIG. 6. Schematic of the energy range of states around the ionization potential. The dark band are those Rydberg states which can be field ionized by the pulsed delayed extraction field. The dashed line shows the ionization potential. These lines are tilted due to the ac Stark shift as a function of laser intensity. The three-photon bandwidth of the laser spectrum of about 200 cm^{-1} is also shown.

spectrum at 610 nm was 3 nm FWHM. After second harmonic generation and a non-resonant three-photon transition, the effective bandwidth is 200 cm^{-1} .) As discussed below, the pulsed extraction field is able to ionize Rydberg states as much as 60 cm^{-1} below the IP. However, the combination of the Stark shift, the range of intensities present in the focal volume, and the large three-photon bandwidth, can also result in excitation to the ionization continuum.

Figure 6 schematically shows the band of Rydberg states that are detectable, and also shows the increase of the IP due to the ac Stark shift. The three-photon bandwidth of the laser is also shown. Depending on the local intensity and the total energy of the three absorbed photons, there are four possible excitations: (1) to a Rydberg state too low to be ionized by the pulsed field, (2) to a Rydberg state which can be field ionized and hence will produce a ZEKE electron, (3) to a continuum state above the IP, and (4) via four-photon ionization to produce a 4 eV electron.

The last two mechanisms can produce a large number of free electrons and ions which have the potential to create space charge effects and hence interfere with the extraction of the Rydberg electrons. If their numbers are small enough, the free electrons will leave the interaction region under the influence of the small static electric field, leaving the Rydberg states to be field ionized by the delayed pulsed field. On the other hand if too many electrons are produced, then they may not be able to escape the space charge, and will be detected at the same time as the true ZEKE electrons. The actual ratios of these various excitations are difficult to estimate, since they require a detailed knowledge of the cross sections, of the pulse shape and of the three-dimensional intensity distribution in the focal volume. Experimental details follow, and more information can be found in Ref. 16.

Xenon was chosen for a variety of reasons: (1) the num-

ber density of neutral Xe atoms in the laser focal volume can be calculated from molecular beam expansion conditions;¹⁷ (2) three-photon non-resonant ionization cross-sections of atomic Xe are well known;¹⁸ (4) high- n Rydberg states converging to the Xe^+ ground state are very long lived and, hence, relatively unaffected by ion-Rydberg interactions;¹⁹ (5) the broad bandwidth of femtosecond pulses allows the simultaneous preparation of high- n Rydbergs and free ions. These experiments allow a separation of electron temperature effects from pure density effects: the electron temperature is constant here.

The experimental set-up, described in more detail elsewhere,¹⁶ is briefly reviewed here. An amplified femtosecond dye laser system produced 500 fs pulses in the $608\text{--}616\text{ nm}$ range. These pulses were spatially filtered to ensure a diffraction-limited spatial profile and then frequency-doubled in an overly long non-linear crystal to yield temporally flat-topped 900 fs pulses (i.e., constant intensity during the pulse) in the $304\text{--}308\text{ nm}$ range. Pulse energies were less than $3\text{ }\mu\text{J}$. For these experiments, the central wavelength of the pulse was tuned approximately 60 cm^{-1} above the ionization potential.

A pulsed nozzle was used to expand pure Xe into the interaction region of a simple photoelectron/photoion spectrometer. The nozzle diameter was $200\text{ }\mu\text{m}$ and the distance to the laser focus was 220 nozzle diameters. The stagnation pressure behind the nozzle was varied from 250 to 1140 Torr , thus giving a range in the number density of Xe atoms in the laser focus of $1.5\text{--}6.9 \times 10^{14}\text{ cm}^{-3}$. It was possible to observe Xe clusters in the mass spectra under certain conditions. The pulsed valve timing was adjusted to ensure that no clusters were present in the beam during these experiments. The detection of ZEKE signals was performed with a pulsed field delay of 500 ns , in the presence of a 2 V/cm offset field and with a pulsed extraction field strength of up to 240 V/cm . This pulsed field was sufficient to ionize Rydberg states that were within 60 cm^{-1} of the IP.

Spatial filtering ensures a known spatial intensity distribution and the flat-topped pulse allows for an approximation of constant intensity during the pulse. In principle, therefore, a simple binning of the pulse energies (measured with a photodiode) allows for a shot-to-shot study of intensity effects. In practice, however, fluctuations in the femtosecond laser pulse duration prohibit this. In order to get around this problem, we use the autocorrelation ratio (ACR)¹⁶ as a data acquisition criterion to select consistent pulse shapes. The ACR is the ratio of the second harmonic pulse energy to the fundamental energy squared, for each pulse. As this ratio depends only on the (spatially averaged) intensity, it is constant for constant pulse duration. Typically, we used a $\pm 10\%$ acceptance filter on the ACR. The laser was focused into a vacuum chamber, described below, using $f/20$ optics.

Typical experiments consisted of binning the ZEKE signal versus laser pulse energy (intensity) at a given gas density. The gas density was then varied systematically. Any plasma effects should appear as a sudden increase in signal. Three examples are shown in Fig. 7. The binning statistics determine that each data point represents $50\text{--}150$ laser shots.

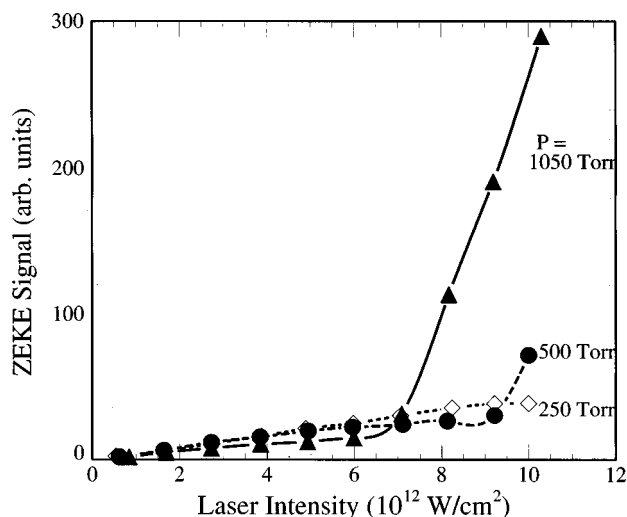


FIG. 7. ZEKE signal measured as a function of laser intensity for a 3-photon interaction with xenon atoms. Several gas pressures are shown. The laser pulses were filtered for constant intensity according to their autocorrelation ratio. The signal has been normalized to the gas pressure. The sharp increase in signal at a threshold intensity I_{crit} is seen to vary as expected for plasma effects: as the density increases, I_{crit} decreases.

With the use of the ACR and the spatial filter, the pulse energy is directly proportional to the average intensity. Towards higher intensity, a dramatic change in slope can be seen in the data: beyond a certain critical intensity, I_{crit} , the ZEKE signal increases much more quickly. This sudden change is due to the turn-on of the plasma trapping of the low energy kinetic electrons at a certain ion density. Table I shows the experimentally inferred values of I_{crit} vs gas pressure. As expected, I_{crit} depends inversely on the density of neutral Xe atoms in the laser focus. It is important to note that trapping of kinetic electrons depends only on the ion density (*N.B.* here the electron “temperature” is invariant) and therefore higher intensities are required to produce the critical ion density when the atomic gas density is reduced.

It is interesting to compare the observed I_{crit} with the estimates from our models. A detailed consideration of the spatio-temporal distribution of intensities in the laser pulse, discussed in detail elsewhere,¹⁶ is not warranted when comparing the results to the simple plasma models presented here. Assume that the interaction takes place in a cylindrical volume with a radius $r_0 = 6 \mu\text{m}$ and a length $\ell = 500 \mu\text{m}$, determined by the laser focus. The density of ions produced by absorption of three photons is

TABLE I. Comparison of I_{crit} , the intensity at which the ZEKE signal starts to rise rapidly, versus backing gas pressure in the pulsed valve. The intensities from the model have used the absorption cross section σ as a free parameter.

Pressure (Torr)	I_{crit} (exp.) (W/cm ²)	I_{crit} (model) (W/cm ²)
250	$> 10^{13}$	1.1×10^{13}
500	9×10^{12}	9×10^{12}
1050	7×10^{12}	7×10^{12}

$$n_e = \sigma I^3 \tau n_0. \quad (13)$$

From eq. (7), the electric field $E_x = 2 \text{ V/cm}$ is less important than the field due to the electrons, i.e., $E_x / (T_e / e r_0) < 1$. Equation (5) gives the fraction of electrons which are able to escape the focal volume due to their kinetic energy. Substituting eq. (13) and setting $f_{esc} = 1$, we get the intensity at which plasma effects become significant,

$$I_{crit} = \left[1.65 \times 10^{14} \frac{T_e (\text{eV})}{r_0^2 (\mu\text{m}) \sigma \tau} \frac{0.13}{6 \times 10^{11} P (\text{Torr})} \right]^{1/3}. \quad (14)$$

We substitute $T_e = 4 \text{ eV}$ (the energy of an electron produced when an atom absorbs a fourth photon), $\tau = 900 \text{ fs}$, and $\sigma = 3.2 \times 10^{-84} \text{ cm}^6 \text{ s}^2$ (from a fit to the data), and obtain

$$I_{crit} (\text{W/cm}^2) = [3.65 \times 10^{41} / P (\text{Torr})]^{1/3}. \quad (15)$$

This model compares well with the experimental values for I_{crit} as shown in Table I. The value of σ inferred is about 30 times smaller than the best available estimates.¹⁸ However, there are a lot of uncertainties in its determination, as there are in the characterization of our intensity. The important point to note is that I_{crit} scales correctly with pressure, giving credence to our model.

ACKNOWLEDGMENT

The authors would especially like to thank Klaus Müller-Dethlefs for originally posing this problem.

APPENDIX A: POTENTIAL OF A CYLINDRICAL CHARGE DISTRIBUTION

In this Appendix we give details about the derivation of eq. (3). The total charge N is assumed to be uniformly distributed in a cylinder of length ℓ and radius r_0 . The electric field near the charge is taken to be the $1/r$ field due to an infinitely long wire. At great distances from the charge the field is taken to scale as $1/r^2$ due to a point charge. The two potentials are matched at some point r_m .

The potentials are given as

$$V_2(r) = -\frac{Ne}{2\pi\epsilon_0\ell} \ln \frac{r_0}{r} + V_0 \quad (A1)$$

and

$$V_3(r) = -\frac{Ne}{4\pi\epsilon_0 r}, \quad (A2)$$

where the former is valid for $r_0 < r < r_m$ and the latter for $r > r_m$. V_0 is a constant required to match the potentials at r_m , so that $V_2(r_m) = V_3(r_m)$.

The energy required to move an electron from $r = r_0$ to $r = \infty$ is calculated by two steps:

$$V_2(r_m) - V_2(r_0) = -\frac{Ne}{2\pi\epsilon_0\ell} \ln \frac{r_0}{r_m} \quad (A3)$$

and

$$V_3(\infty) - V_3(r_m) = \frac{Ne}{4\pi\epsilon_0 r_m}. \quad (\text{A4})$$

The energy difference is

$$\Delta V = V_3(\infty) - V_2(r_0) = \frac{Ne}{4\pi\epsilon_0} \left(\frac{1}{r_m} - \frac{2}{\ell} \ln \frac{r_0}{r_m} \right). \quad (\text{A5})$$

If we take the matching point to be $r_m = \ell$, and if we equate $\Delta V = T_e/e$, then

$$N = \frac{4\pi\epsilon_0 T_e \ell}{e^2} \frac{1}{1 + 2\ln \ell / r_0}. \quad (\text{A6})$$

APPENDIX B: PARTICLE-PARTICLE SIMULATION DETAILS

Here we want to calculate the exact force on each particle, namely

$$\vec{F}_i = \sum_{j \neq i} \frac{q_i q_j \vec{r}_{ij}}{4\pi\epsilon_0 r_{ij}^3} + q_i \vec{E}_{ext}. \quad (\text{B1})$$

The problem of a large number of interacting particles is the general N -body problem which has no exact solution. Various methods exist which are highly accurate and which are used, for example, to calculate the evolution of galaxies.²⁰ For instance, the Aarseth method²¹ is a fourth order predictor-corrector method which is widely used. In the present case, we are not as much interested in the detailed evolution of the plasma as we are in how many particles escape, and so there is not much to be gained by the much more complex high order solvers. Therefore we elected to use a fast first order solver. The same code was used with a fourth order solver to do molecular ionization calculations in intense laser fields.²²

Each particle i is represented by a three-dimensional position \vec{r}_i and a three-dimensional velocity \vec{v}_i . As is usual for computer calculations, normalized units are used. This ensures that quantities are of order one, and enables one calculation to apply to a large number of real parameters. We use primed quantities here to refer to the normalized variables,

$$x' = x/\lambda_D, \quad (\text{B2})$$

$$t' = t\omega_p, \quad (\text{B3})$$

$$E' = E \frac{\epsilon_0}{en_e \lambda_D}, \quad (\text{B4})$$

$$\lambda_D = \left(\frac{\epsilon_0 T}{n_e e^2} \right)^{1/2}, \quad (\text{B5})$$

$$\omega_p = \left(\frac{n_e e^2}{m_e \epsilon_0} \right)^{1/2}. \quad (\text{B6})$$

Here λ_D is the Debye length, ω_p is the plasma frequency, n_e is the electron number density and T is the temperature of the electrons in energy units.

In order to simulate a random distribution of ion-electron pairs, the fixed ions were randomly distributed in space, and an electron was placed close to its ion with a kinetic energy such that it could escape the ion's potential and then have random energy T .

The quantities were advanced at each time step, using the time-centered leapfrog method. Here we use normalized quantities but have dropped the prime symbols for clarity,

$$\vec{r}_i^{n+1} = \vec{r}_i^n + \vec{v}_i^{n+1/2} \Delta t, \quad (\text{B7})$$

$$\vec{v}_i^{n+3/2} = \vec{v}_i^{n+1/2} + \vec{F}_i \Delta t / m. \quad (\text{B8})$$

Here, superscript n refers to the time step $t = n\Delta t$, and subscript i refers to the i -th particle.

The external field is turned off initially, and after several hundred time steps it is ramped up to its full value. This is to allow the particles to reach equilibrium with the self-consistent field, since their initial distribution within the slab is not an equilibrium distribution.

The code was tested with two particles to verify that it correctly calculated orbits and escape trajectories, and that it conserved energy. As is common in N -body calculations, the force term in eq. (B1) is truncated at some minimum r so that very high accelerations are avoided. However, ‘‘recombination’’ of electrons with ions was observed, as some electrons became trapped in orbits about ions.

APPENDIX C: PARTICLE-IN-CELL SIMULATION DETAILS

The particle-in-cell method is similar to the particle-particle method, except in how the field is calculated. Instead of calculating the field at each particle's position, a spatial grid is used to store the field, and the field experienced by each particle is interpolated from this grid. This model was limited to one dimension because of the integration technique used to calculate the field; higher dimensions are possible using Fourier methods.

Each simulation ‘‘particle’’ represents a sheet of charge. The charge that it represents is chosen so that the initial distribution has density n_e . The initial distribution is set up as a slab of some thickness with the particles uniformly distributed across it. The ions are taken to be a fixed, uniform density across the slab. The particles are given random initial velocities with a Maxwellian distribution. (Various distributions shapes were tried, such as rectangular distributions, but these had no effect on the number of escaped particles.)

The N particles' positions x_i and velocities v_i are kept as vectors at each time step. The electric field is calculated on a fixed spatial grid with grid size $\Delta x = 0.2\lambda_D$ by counting the number of particles which lie in each grid, using triangular interpolation. This grid is then used to calculate the self-consistent electric field, to which is added the applied external field.

At each time step $\Delta t = 0.125\omega_p^{-1}$ the positions and velocities are calculated using the time-centered leapfrog method. Here we use the normalized quantities but have dropped the prime symbols for clarity:

$$x_i^{n+1} = x_i^n + v_i^{n+1/2} \Delta t, \quad (\text{C1})$$

$$E_j^{n+1} = \int_0^{j\Delta x} n dx, \quad (\text{C2})$$

$$v_i^{n+3/2} = v_i^{n+1/2} - E_j^{n+1} \Delta t. \quad (\text{C3})$$

Here, superscript n refers to the time step $t = n\Delta t$, subscript i refers to the i -th particle and subscript j refers to the spatial position $x = j\Delta x$.

Usual numerical tests were made to confirm the accuracy of the results: Δt and Δx were halved, the number of particles N was doubled, the thickness of the initial slab was varied, different initial velocity distributions were tried, etc.

- ¹G. Reiser, D. Rieger, T. G. Wright, K. Muller-Dethlefs, and E. W. Schlag, *J. Chem. Phys.* **97**, 4335 (1993).
²K. Muller-Dethlefs and E. W. Schlag, *Annu. Rev. Phys. Chem.* **42**, 109 (1991).
³A. Strobel, I. Fischer, A. Lochschmidt, K. Muller-Dethlefs, and V. E. Bondybey, *J. Phys. Chem.* **98**, 2024 (1994).
⁴J. M. Smith, C. Lakshminarayan, and J. L. Knee, *J. Chem. Phys.* **93**, 4475 (1990).
⁵T. Baumert, R. Thalweiser, and G. Gerber, *Chem. Phys. Lett.* **209**, 29 (1993).

- ⁶I. Fischer, D. M. Villeneuve, M. J. J. Vrakking, and A. Stolow, *J. Chem. Phys.* **102**, 5566 (1995).
⁷M. C. R. Cockett, J. G. Goode, K. P. Lawley, and R. J. Donovan, *J. Chem. Phys.* **102**, 5226 (1995).
⁸F. Merkt and R. N. Zare, *J. Chem. Phys.* **101**, 3495 (1994).
⁹M. J. J. Vrakking and Y. T. Lee, *Phys. Rev. A* **51**, R894 (1995).
¹⁰M. J. J. Vrakking, I. Fischer, D. M. Villeneuve, and A. Stolow, *J. Chem. Phys.* **103**, 4538 (1995).
¹¹M. Yu. Ivanov and A. Stolow, *Chem. Phys. Lett.* **265**, 231 (1997).
¹²R. W. Hockney and J. W. Eastwood, *Computer Simulation Using Particles* (McGraw-Hill, New York, 1981).
¹³C. Alt, W. G. Scherzer, H. L. Selzle, and E. W. Schlag, *Chem. Phys. Lett.* **224**, 366 (1994).
¹⁴X. Zhang, J. M. Smith, and J. L. Knee, *J. Chem. Phys.* **99**, 3133 (1993).
¹⁵W. A. Chupka, *J. Chem. Phys.* **98**, 4520 (1993).
¹⁶A. Zavriyev, I. Fischer, D. M. Villeneuve, and A. Stolow, *Chem. Phys. Lett.* **234**, 281 (1995).
¹⁷G. Scoles, *Atomic and Molecular Beam Methods* (Oxford University Press, Oxford, 1992).
¹⁸I. Schechter, H. Schroder, and K. L. Kompa, *Chem. Phys. Lett.* **194**, 128 (1992).
¹⁹M. J. J. Vrakking and Y. T. Lee, *J. Chem. Phys.* **102**, 8833 (1995).
²⁰*Multiple Time Scales*, edited by J. U. Brackbill and B. I. Cohen (Academic, Orlando, 1985).
²¹S. J. Aarseth, *Astrophys. Space Sci.* **14**, 118 (1971).
²²D. M. Villeneuve, M. Yu. Ivanov, and P. B. Corkum, *Phys. Rev. A* **54**, 736 (1996).